ACS APPLIED MATERIALS & INTERFACES

www.acsami.org

Research Article

Digitally Tuned Copper Composites: From Oxide-Free Encapsulation to Graphene Hybrids

Dmitry Cheshev, Sergey Kaprov, Andrey Averkiev, Maxim Fatkullin, Konstantin Brazovskiy, Raul D. Rodriguez,* and Evgeniya Sheremet

Cite This: https://doi.org/10.1021/acsami.5c17459

Read Online

ACCESS | Metrics & More | Article Recommendations | Supporting Information

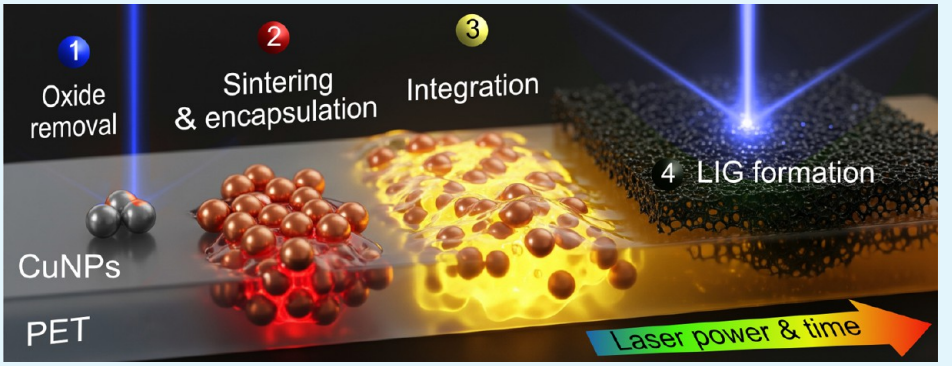

ABSTRACT: We present a tunable manufacturing platform for copper nanoparticles (CuNPs) on polyethylene terephthalate (PET) that addresses the critical challenge of processing this air-sensitive material under ambient conditions. By precisely controlling laser parameters, we demonstrate that a single CuNPs-PET precursor can produce two distinct functional composites. Low laser powers result in a purely metallic composite within the polymer matrix by simultaneously sintering and encapsulating CuNPs. In contrast, higher laser powers shift the process toward polymer carbonization and graphitization, creating a durable copper-assisted laser-induced graphene (Cu-LIG) hybrid embedded in PET. High-speed visualization enables real-time analysis of the mechanisms involved, revealing the sintering, encapsulation, and integration of CuNPs into the polymer. Chemical and structural analyses show that the laser process also reduces native copper oxide on pristine NPs, resulting in a metallic copper composite with a sheet resistance as low as 0.13 Ω sq^{-1} and significant stability under harsh conditions, including exposure to high relative humidity (RH) levels above 95% for several days. We demonstrate practical applications of these composites by creating highly robust, flexible devices, including thermocouples with a Seebeck coefficient of 14.6 $\mu V\ °C^{-1}$ and high-load capacitive pressure sensors. This work redefines laser processing as a versatile approach for digitally selecting material functionality, advancing the manufacturing of flexible electronics.

KEYWORDS: *laser processing, copper nanoparticles, high-speed recording, laser-induced graphene, flexible thermocouple*

INTRODUCTION

Laser processing of nanomaterials on polymer substrates is an emerging method for flexible electronics, offering scalability, precision, maskless digital fabrication, and cost-effectiveness.[1−3] One of the most promising methods is selective laser sintering (SLS) of metallic nanoparticles, which allows for the local creation of conductive pathways. SLS's versatility comes from adjusting laser processing parameters, enabling the modulation of conductivity and the production of various flexible devices, such as strain sensors, temperature sensors, and antennas. However, poor mechanical stability and adhesion of these structures remain significant challenges in digital SLS, making them susceptible to failure under bending, abrasion, or environmental exposure, which are common in real-world applications of flexible electronics.

To address this, our group previously established the fundamental components for the laser-driven integration of nanomaterials into polymer substrates. This approach allows the creation of ultrarobust metal−polymer composites, initially demonstrated by Rodriguez et al., who used aluminum nanoparticles on polyethylene terephthalate (PET) to produce a resilient Al-LIG hybrid.[4] The mechanistic understanding of this process was later clarified by Abyzova et al. through high-

Received: September 26, 2025
Revised: December 15, 2025
Accepted: December 16, 2025

speed recordings, which revealed the complex melt pool dynamics and Marangoni flows responsible for physically integrating reduced graphene oxide (rGO) into various thermoplastic polymers.[5] Additionally, this concept was successfully extended to other metallic nanomaterials like silver nanoparticles, resulting in the development of flexible electrochemical sensors.[6]

Copper is an essential material for flexible electronics because of its low cost and high electrical conductivity, especially when combined with laser processing.[7−12] However, applying this method to copper nanoparticles (CuNPs) introduces several challenges, such as low mechanical stability, vulnerability to oxidation in ambient conditions that reduces electrical conductivity, and potential damage to the polymer substrate from photothermal effects during SLS.[13−15] These problems greatly limit the feasibility of using laser-processed CuNPs in flexible electronics.

The low mechanical stability of sintered CuNPs results from weak adhesion to polymeric substrates and the fragility of the sintered layers.[16,17] Despite their high porosity and surface area, the actual contact with the substrate is much smaller due to voids within the sintered layer. This leads to weaker adhesion than with uniform coatings, such as those produced by sputtering. However, high sputtering temperatures can damage temperature-sensitive polymers. One way to address this is to use plasma treatment to improve adhesion, which has been shown to enhance the mechanical stability of various nanoparticle systems.[7−10] Alternatively, employing polymers as a bonding layer can also boost adhesion. For example, using polyvinylpyrrolidone (PVP) as both a stabilizer and adhesive increased the contact area and facilitated the formation of a dense CuNPs film.[18] Polymers can also serve as protective layers over conductive structures, strengthening sintered layers, reducing detachment from the polymer substrate,[19] and preventing oxidation of the sintered structures. This is especially important for CuNPs, which tend to oxidize under ambient conditions.[19] While most research focuses on polymer capping layers on isolated CuNPs, applying polymer coatings on sintered nanoparticle structures is still largely unexplored. A promising approach to improve substrate adhesion involves raising the substrate polymer's temperature to its glass transition point, creating an interface layer between the substrate and the sintered nanoparticles deposited on it.[20]

A successful process must accomplish the following: 1) nanoparticle sintering for conductivity, similar to SLS; 2) in situ reduction of native oxides; 3) strong substrate adhesion, as achieved on a heating plate; and 4) nanoparticle encapsulation that protects it from the environment. Ideally, all these steps should occur simultaneously in a single scalable process. Additionally, the potential to harness photothermal and photochemical effects to turn the laser into a controllable switch, capable of producing various material endpoints from a single nanoparticle precursor, remains unrealized.

In this work, we aim to bridge this gap by developing a laser-based method for fabricating copper nanoparticle structures on PET. We show that by carefully controlling the laser-thermal regime, we can overcome all the CuNPs processing challenges mentioned earlier. This level of control allows the conversion of the precursor into two functional materials: a pure, oxide-free, encapsulated Cu composite with a sheet resistance of 0.13 Ω sq^{-1}, and a copper-graphene hybrid (Cu-LIG). The encapsulation greatly protects the sintered copper structures from harsh environmental conditions, including high humidity (relative humidity > 95%) and high temperature (70 °C). In contrast, sintered-only structures without encapsulation oxidized and delaminated from the substrate after 10 days of exposure to RH > 95% at 40 °C. However, the encapsulated structures stayed conductive, with sheet resistance ranging from 1.8 Ω sq^{-1} to 40 Ω sq^{-1}. Beyond their outstanding environmental stability, we demonstrate the functionality of these Cu composites by creating multimaterial flexible thermocouples made from NiNPs/CuNPs and CuNPs/Cu-LIG, achieving thermoelectric coefficients of 14.6 μV $°C^{-1}$ and 5.1 μV $°C^{-1}$, respectively, along with a high-load pressure-capacitive sensor measuring 0.1 kg changes. This work shifts traditional laser processing from a single-result process to a versatile method for digital manufacturing of high-performance Cu-based materials for flexible electronics. Our laser-based approach allows various material transformations that are easily controlled by adjusting the laser power, as shown in Figure 1a.

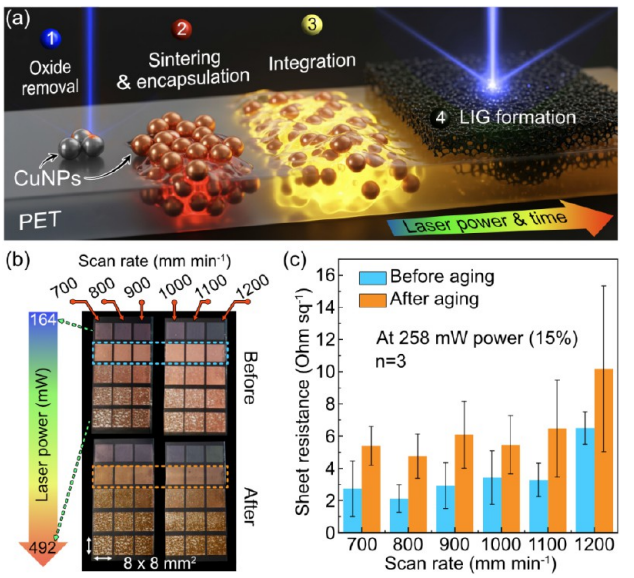

Figure 1. (a) Controllable laser-driven platform for Cu and Cu-laser-induced graphene (LIG) hybrid composites, where the laser intensity and time drive a single CuNP-on-PET precursor through different materials and stages: (1) Oxide removal, (2) Sintering & encapsulation, (3) Full polymer integration, and (4) Cu-assisted LIG formation. (b) Sample photographs and (c) sheet resistance of samples before and after exposure to high humidity >95% RH for 3 days. The encapsulated structures retained a copper-like (metallic) appearance after the humidity-stress test. In contrast, the sintered-only structures delaminated from the substrate or reverted to a black color due to reoxidation. The dashed rectangles in (b) indicate the squares from which the sheet-resistance values presented in (c) were measured.

First, we demonstrate the exceptional stability of the composites, then explain the mechanisms behind moderate-intensity encapsulation and high-intensity graphitization, and finally evaluate their performance in flexible device applications.

RESULTS AND DISCUSSION

Overcoming Environmental Stability Issues. The main challenges in conventional laser processing of Cu nanostructures are their poor adhesion to the substrate and their tendency to oxidize. To address this, two main strategies have

https://doi.org/10.1021/acsami.5c17459
ACS Appl. Mater. Interfaces XXXX, XXX, XXX−XXX

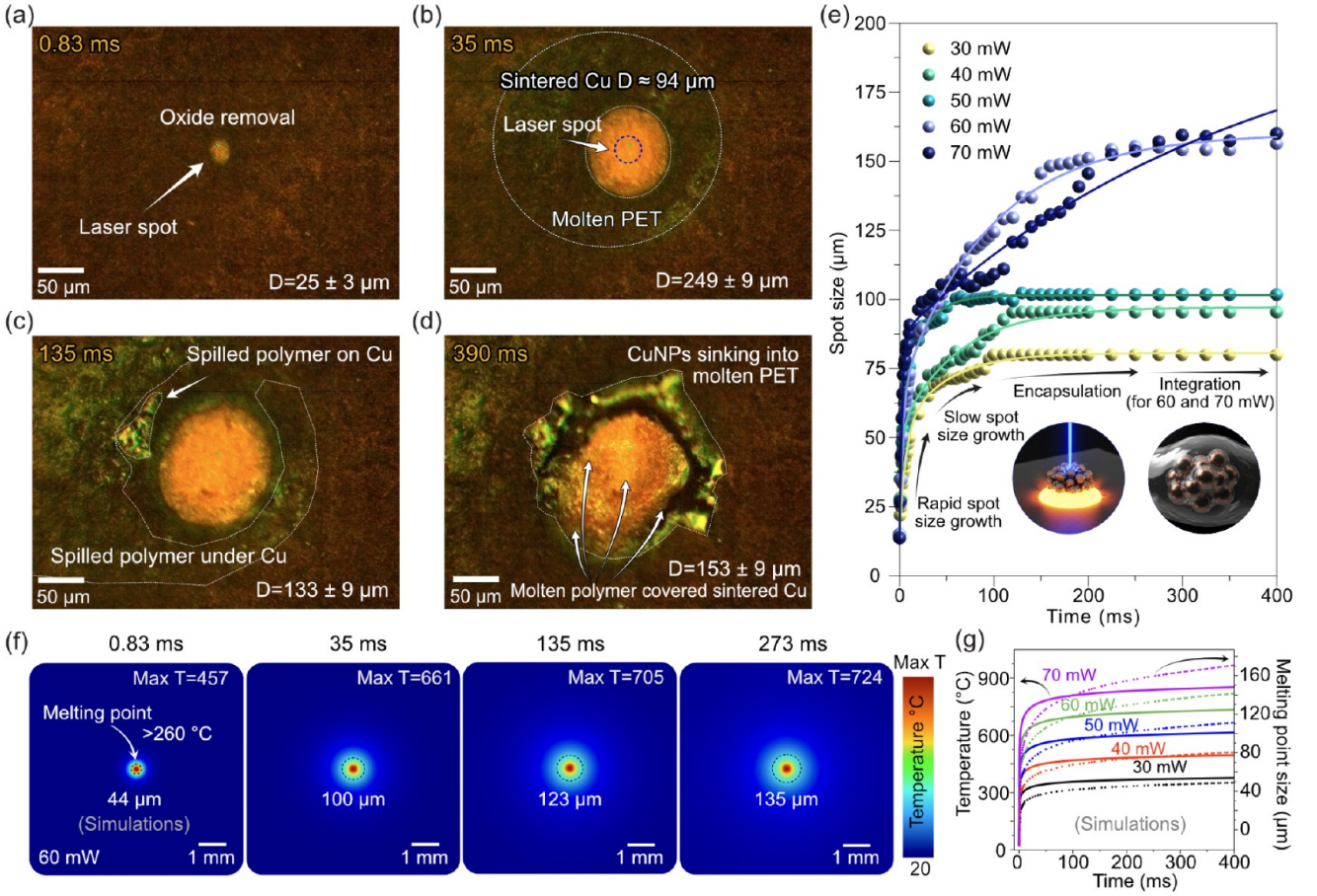

Figure 2. Time-resolved experimental and computational analysis of the encapsulation mechanism. (a–d) Key frames from high-speed imaging (60 mW laser) provide direct experimental evidence of the process, showing initial oxide removal, sintering, and the eventual encapsulation as CuNPs sink into the molten PET. (e) The experimentally measured spot size over time reveals stages of rapid growth, slow growth, encapsulation, and integration, as illustrated in the inset. (f) FEM simulations of the temperature distribution and (g) the corresponding maximum temperature (solid lines, left axis) and melt pool diameter (dashed lines, right axis) provide a theoretical explanation for the observed phenomena, showing excellent agreement with the experimental data.

been reported: chemical passivation with 3-mercaptopropyltrimethoxysilane[21] and formates,[22] or physical encapsulation with PMMA[23] and CVD graphene.[24] Indeed, graphene shielding of CuNPs through thermal decomposition of PVP and using CVD graphene has been demonstrated in several studies.[25−27] However, these approaches seldom address mechanical robustness issues, often requiring additional steps such as oxygen plasma treatment or mechanical pressing,[28−30] which increase complexity and costs in flexible device fabrication. Furthermore, these processes typically require an inert atmosphere and are primarily demonstrated for powders or 3D copper structures, while their use on CuNPs films on temperature-sensitive polymers remains limited.

In contrast, our simple single-step method uses CuNPs "as is" and addresses stability and adhesion issues simultaneously via laser-induced encapsulation.

We validated our method by subjecting sintered CuNPs, with and without polymer encapsulation, to accelerated aging under harsh conditions: at 70 °C with a relative humidity (RH) of >95% for 3 days, and at 40 °C with RH of >95% in an environmental chamber for 10 days. The results with different levels of CuNP encapsulation and integration on PET were obtained by adjusting the laser power and scan speed (see Figure 1b). The sheet resistance (R_S) measured for each square (see Figure 1c) served as the metric for copper degradation.

Initially, the sheet resistance R_S of the laser-processed structures in Figure 1b ranged between 0.5 and 6 Ω sq^{-1}. After 3 days of accelerated aging, encapsulated Cu structures exhibited good stability when cycling between harsh and mild conditions, retaining a sheet resistance ranging from 3.4 ± 1.7 Ω sq^{-1} (the initial sample) to 5.5 ± 1.8 Ω sq^{-1} (after aging), all without the use of additional protective measures. After 10 days in the environmental chamber (40 °C, RH > 95%), the sintered-only samples (red−pink) delaminated due to condensed water, whereas the encapsulated samples (brown) remained largely intact (see Figure S1). Before the environmental chamber, encapsulated CuNPs exhibited R_S values ranging from 0.5 Ω sq^{-1} to 2 Ω sq^{-1}, corresponding to resistivities of 0.5 mΩ cm and 2 mΩ cm, respectively, assuming a ≈ 10 μm CuNPs/PET layer thickness (determined from cross-sectional SEM data in Figure 3). The lowest R_S recorded was 0.13 Ω sq^{-1}. After the environmental chamber, the R_S of the brown squares increased to between 1.8 Ω sq^{-1} (1.8 mΩ cm) and 40 Ω sq^{-1} (40 mΩ cm), as seen in Figure S1. R_S values for all structures are listed in Table S1. For comparison, resistivity values reported for SLS of CuNPs are in the μΩ cm range, which is lower than that of our encapsulated CuNPs.[31−33] Despite this higher resistivity, the stability of these conductive structures under high RH and elevated

https://doi.org/10.1021/acsami.5c17459
ACS Appl. Mater. Interfaces XXXX, XXX, XXX−XXX

temperatures highlights the potential of the encapsulation approach for durable, cost-effective flexible electronics.

We benchmarked our strategy by comparing stability metrics with reported CuNP protection methods. Kwon et al. found that 3-mercaptopropyl-trimethoxysilane preserved Cu's electrical properties for 15 days in ambient conditions.[21] Formate also showed anticorrosion effects, allowing Cu to retain conductivity after 1 day in 0.1 M NaOH with a $\Delta R/R_0$ change below 1% after 30 days in ambient air.[22] PMMA-encapsulated Cu nanowires (CuNWs) resisted rapid degradation in air when used as heaters.[23] Meanwhile, CVD graphene-protected CuNWs achieved a $\Delta R/R_0$ below 0.2 after 180 days in ambient conditions.[24] In comparison, our encapsulated samples exhibited a $\Delta R/R_0$ between 0.8 and 26.7. While these changes are greater than those reported for tests in ambient air, our results were obtained under significantly more extreme conditions (RH > 95%, 40−70 °C). This confirms the benefits and versatility of our method, which rivals other complex approaches by providing robust protection without the need for additional protective steps or treatments.

We hypothesized that the increase in resistance was due to partial oxidation of the conductive copper network. The best samples retained resistance values close to the initial ones, thanks to the PET shielding, which protected the majority of the Cu conductive paths from the oxidative environment. We verified this protection mechanism using Raman microscopy, recording spectra on the most degraded sample. Optical microscopy imaging revealed green inclusions, indicating oxidation of the copper network (Figure S2a). Raman spectra of these inclusions confirmed the presence of Cu_2O and CuO (Figure S2b). These oxides were also detected in spectra from the initial CuNPs film and non-laser-treated films after aging (Figure S2c−d). Conversely, the sample exhibiting minimal changes in R_S showed no detectable copper oxide peaks in its Raman spectra (Figure S2e), displaying only the photoluminescence (PL) background of laser-processed PET.[34] These observations indicate that although CuNPs in the presence of PVP get reduced by laser irradiation, poor integration into the polymer substrate leaves exposed metallic copper vulnerable to moisture, resulting mainly in the formation of Cu_2O, resulting in as much as a 20-fold increase in sheet resistance. However, proper encapsulation shields the conductive Cu network, preventing oxidation and confirming PET's protective effect.

The Mechanism of Laser-Induced Encapsulation and Integration. The samples used for the environmental stability tests were produced using a pulsed laser, given the widespread accessibility of such devices. However, to investigate the encapsulation and integration mechanisms with greater temporal precision, we switched to a continuous-wave laser. We confirmed that this change did not compromise environmental stability (Figure S1), allowing us to precisely resolve the dynamics of laser-CuNPs/PET interactions within the millisecond time scale while maintaining the desired level of stability.

The exceptional reliability and stability of these composites result from the "sinter-then-encapsulate" process. We captured this process in real time with a high-speed camera (1200 fps) mounted on an optical microscope. Figure 2a−d display key frames from a 60 mW CW laser process using a single 30 × 30 μm^2 top-hat laser beam. The complete high-speed recording, at 1200 fps with an 830 μs exposure time, is available as Supporting Video 1.

We identified different stages shown in Figure 1: Oxide removal (1 ms), Sintering (0−35 ms), Encapsulation (35−150 ms), and Integration (150+ ms). An orange spot appeared on the film surface, indicating the start of oxide removal and CuNPs sintering within 1 ms of laser irradiation (Figure 2a). The estimated spot size is 25 ± 3 μm, matching the laser beam size. Over the next 5 ms, the sintering area quickly doubled in diameter. The growth of sintered CuNPs continued for about 35 ms, but the growth rate decreased exponentially. Additionally, PET melting became more noticeable, shown by the yellow-green areas near the spot (Figure 2b), caused by the blue laser reflecting off the melt pool and the PET's photoluminescence.[35] The size of this area is larger than that of the sintered nanoparticles due to thermal energy transfer from the laser to the surroundings, with CuNPs acting as the main heat transfer medium because of their higher thermal conductivity than PET.[36] After 35 ms, the sintering process slowed down and stabilized between about 100−250 ms, depending on laser power. During this period, molten polymer spreads due to Marangoni flows, covering the CuNPs film near the spot. At 100−150 ms, the molten polymer encapsulated the sintered Cu, as shown in Figure 2c.

Multiple experiments showed that the process duration depends on the laser power and film quality, including the presence of cracks, thickness, and partial flake integration. Once encapsulated, convective flows in the melt pool help sink nanoparticles into the pool, thereby incorporating them into the polymer. This process, which begins after 150 ms, is marked by the defocusing of the sintered NPs and can indicate integration, as shown in Supporting Video 2. Integration was mainly observed at laser powers between 60 mW and 70 mW, while sintering and encapsulation dominate at 30−50 mW. Therefore, three stages of CuNP laser processing on PET can be identified: sintering, encapsulation, and integration, as depicted in Figure 1a. Similar processes were also observed for NiNPs irradiated under the same conditions at powers from 90 mW to 160 mW (see Figure S3). Larger laser powers were required for NiNPs due to their higher sintering temperatures of 800−850 °C, compared to 300−400 °C for CuNPs.[2,37]

To estimate temperature from laser irradiation, we used finite element method (FEM) simulations. Figure 2f displays the in-plane temperature gradient for different laser irradiation times. The model shows a rapid temperature rise within the first millisecond, followed by a moderate increase over 400 ms (Figure 2g). The melting pool diameter was estimated in Figure 2f,g based on the 260 °C melting point of PET,[38] revealing the most significant growth within the first 50 ms. The growth rate of the pool slowed over the following 400 ms. The simulation results closely match the experimental data; however, the experiments indicate a slightly faster melt pool expansion, likely due to flake tilting, integration, or film inhomogeneity. The computational model does not account for dynamic changes in thermal conductivity and optical absorption during CuNPs sintering. Nonetheless, the optical absorption of CuNPs after sintering remains relatively stable at a laser wavelength of 450 nm. As shown in Figure S4, the CuNPs powder absorbs all incident light at this wavelength, with absorption decreasing to 98.5% after sintering.

Next, we explored laser-induced encapsulation and integration by scanning the CuNPs on PET at 5 mm s^{-1} under the laser beam while recording high-speed videos (see Supporting Video 3). Given its size and scanning speed, the beam should impact each point for about 6 ms, which is enough for

https://doi.org/10.1021/acsami.5c17459
ACS Appl. Mater. Interfaces XXXX, XXX, XXX−XXX

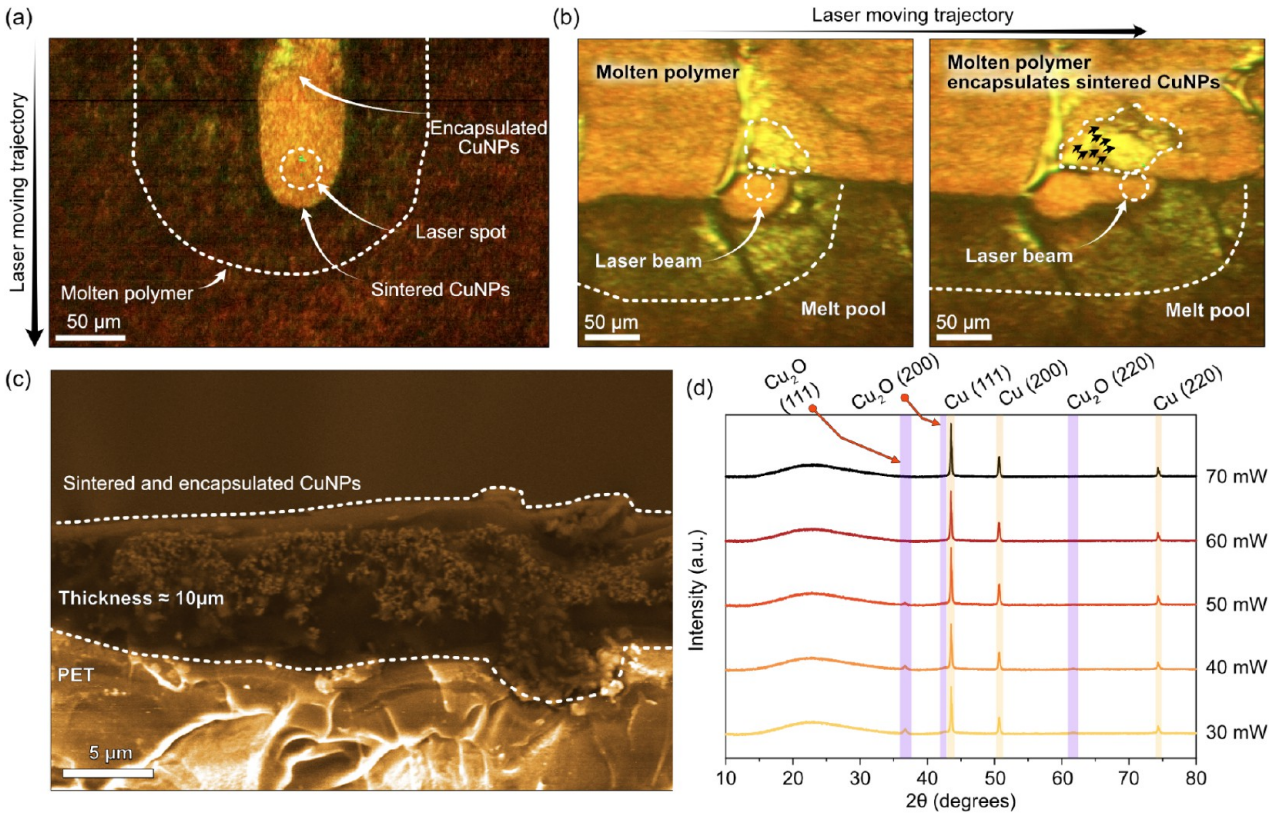

Figure 3. Encapsulation of sintered structures into PET. (a) Encapsulation of sintered CuNPs behind the laser spot on a single line. (b) The laser melts the polymer, which is then spilled onto already sintered structures, encapsulating them. (c) Cross-section SEM image of sintered CuNPs/PET composite integrated in PET. (d) XRD patterns of sintered CuNPs reveal that the oxide species content decreases with power.

nanoparticle sintering but not for encapsulation and integration. However, we noticed that molten polymer covered the sintered structures behind the laser path during single-line patterning (see Figure 3a and Supporting Video 3). Additionally, the polymer melts ahead of the laser beam due to heat transfer, which we used for line-by-line laser processing, as shown in Figure 3b and corresponding high-speed video (Supporting Video 4). The molten polymer ahead of the beam encapsulates the previously sintered CuNPs structures, confirmed by cross-sectional scanning electron microscopy (SEM) in Figure 3c, indicating the formation of a composite up to 10 μm thick.

X-ray diffraction patterns of the newly formed CuNPs/PET composite were recorded to analyze the phase composition of the nanoparticles. Figure S5 shows results for pristine CuNPs powder with Cu (reflexes {111}, {200}, and {220}) and oxides: CuO ({002}, {111}, {202}, {002}) and Cu_2O ({111}, {200}, {220}, and possibly {311} overlapping with Cu {220}). The overlap between the Cu_2O {311} and Cu {220} peaks in the 74.2°−74.5° range is common and has been documented before.[39] The presence of both CuO and Cu_2O comes from the original NPs, which contain both phases, as confirmed by Raman spectroscopy data presented in Figure S2c. XRD patterns of CuNPs/PET composites created with different laser power showed that reflexes from CuO disappeared, indicating Cu reduction, with only the Cu_2O {111} reflex detected at 30−50 mW, while Cu_2O {200} and Cu_2O {220} reflexes were weaker. As the laser power increased, the Cu_2O {111} peak intensity decreased and disappeared at 60 mW. Simultaneously, signals for Cu_2O {200} and Cu_2O {220} planes became barely visible at 40 mW and disappeared at 50 mW. At 60 mW and 70 mW, the CuNPs/PET composites consisted of oxide-free sintered CuNPs with the dominant Cu {111} plane and fewer Cu {200} and Cu {220} planes, indicating a photothermal phase transition.

Copper oxide reduction during laser processing can occur due to high temperatures and the use of PVP as a stabilizing and reducing agent during decomposition under laser irradiation. FEM simulations show that the maximum temperature at 60 mW laser power is around 650 °C, which is below the temperatures required for CuO and Cu_2O to reduce Cu (above 1000 °C).[40] Therefore, we conclude that photothermal decomposition of PVP is the main factor in reducing copper oxide. Lee et al. and Ryu et al. demonstrated that PVP decomposition products released during exposure to laser or intense light pulses can reduce copper oxides.[41,42] The mechanism involves PVP breaking down into alcohols, acids, and gases (methylene, methylamine, and CO_2). Alcohols and acids reduce copper(I, II) oxides to metallic copper, and the high temperatures generated by laser irradiation enhance this reduction. The gases released protect the metal from reoxidation until the polymer encapsulates the Cu nanostructures.

The Tunable Platform: Switching to a Cu-LIG Hybrid at High Intensities. Laser-induced graphene (LIG) formation is another method for creating conductive, flexible devices, typically from polymers such as polyimide (PI), which are rich in aromatic structures. The process involves laser-induced pyrolysis of the polymer, leading to structural reconstruction and LIG development, along with some amorphous carbon. Compared to PI as a LIG precursor, PET, which has fewer aromatic rings, results in greater

https://doi.org/10.1021/acsami.5c17459
ACS Appl. Mater. Interfaces XXXX, XXX, XXX−XXX

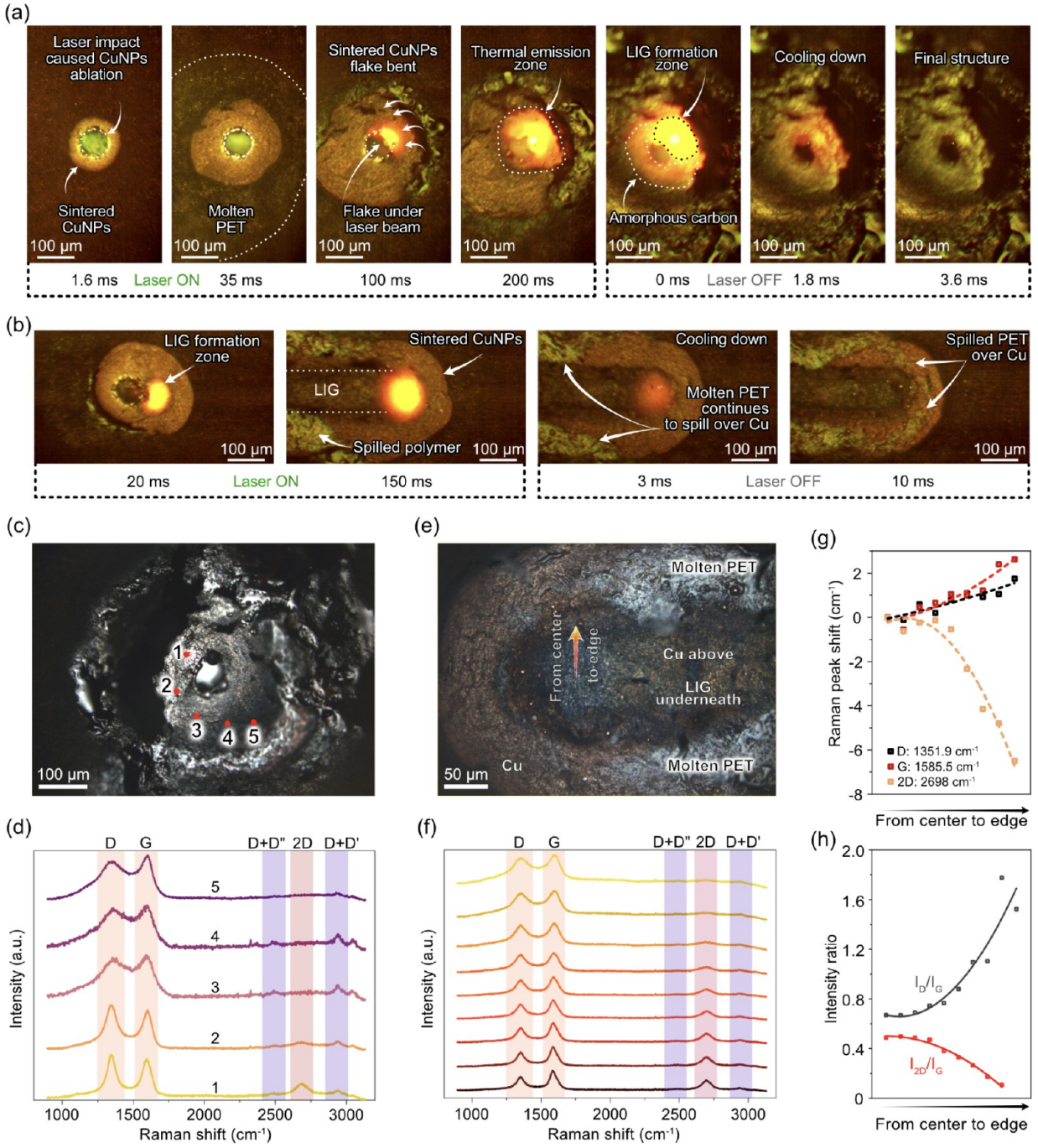

Figure 4. LIG formation out of CuNPs coated on PET. Time-resolved laser processing of CuNPs on PET at high laser power at one spot (a) and during line engraving (b). The thermal emission zone correlates with the LIG-containing area, indicating PET graphitization. (c) Optical microscopy image of carbonized polymer spot with (d) corresponding Raman spectra demonstrating carbon nanomaterial structure changes over different locations. (e) Optical microscopy of a laser line with (f) Raman spectra recorded along the center to the line's edge. (g) D, G, and 2D Raman peaks shift, and (h) I_D/I_G and I_{2D}/I_G peak intensities ratio demonstrates LIG structure changes moving from the center of the line to its edge as marked in (e).

production of amorphous carbon. CuNPs serve as efficient photothermal transducers because of their strong absorption in the blue spectral range, something PET alone cannot do due to its optical transparency. After sintering, CuNPs exhibit an absorption peak at 450 nm (Figure S4), which matches the laser wavelength used in this work.

To initiate LIG formation, the laser's optical power and density were greatly increased compared to the previous CuNPs sintering case. The process was first studied using a high-speed camera when the laser was stationary and during scanning. Snapshots from high-speed recordings of both experiments are shown in Figure 4, and the full videos are available in Supporting Video 5.

We start by examining a single spot, as shown in the time-resolved process in Figure 4a. When the laser hits the sample's surface, three processes occur: first, CuNPs are ablated directly beneath the beam; second, the surrounding areas sinter and grow within 35 ms; and third, the underlying polymer melts.

https://doi.org/10.1021/acsami.5c17459
ACS Appl. Mater. Interfaces XXXX, XXX, XXX−XXX

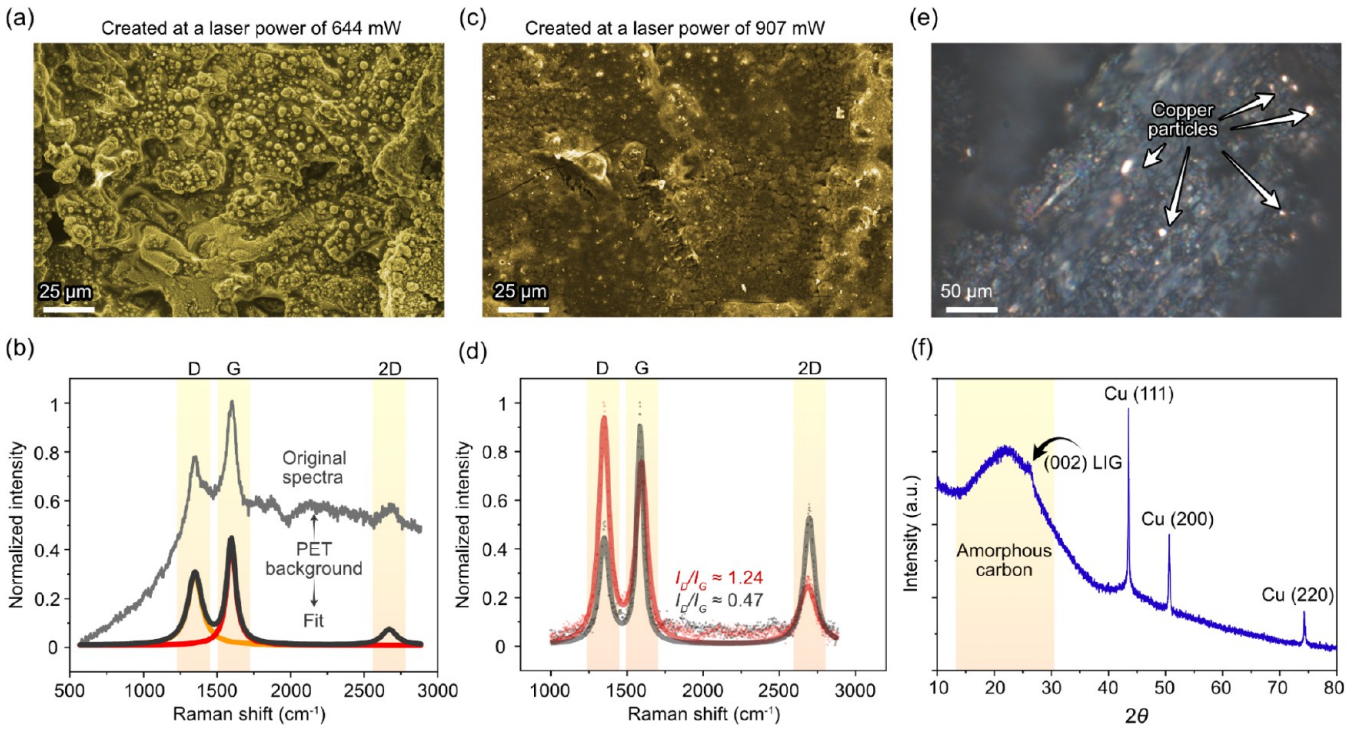

Figure 5. Morphology and content of large-scale Cu-LIG composites. (a) SEM image of Cu-LIG sample morphology with (b) corresponding Raman spectra of LIG overlapped with background signal from PET. (c) SEM image of Cu-LIG sample morphology with (d) corresponding Raman spectra revealing differences (I_D/I_G ratios) in LIG quality. (e) Optical microscopy image demonstrates Cu particles incorporated into the composite. (f) The XRD pattern confirms the presence of metallic Cu, with no oxide species detected.

Convective flows in the molten polymer cause sintered CuNPs to move, with some particles entering the laser beam within approximately 100 ms, as shown by bright thermal emission. The emission zone expands, with the highest brightness directly at the laser impact point and decreasing brightness toward the edges of the spot. The laser is turned off after 1 s of irradiation, causing the thermal emission to disappear within 4 ms (shown in Figure 4a in the "Laser OFF" block). In Figure 4a, the thermal emission area, outlined with a dashed line, shows a yellow-white gradient at the laser-impact zone and an orange-red gradient at the edges, indicating different temperatures.

We recorded Raman spectra at five points along the edge to analyze the structure of the newly formed carbon and its spatial variations around the laser spot. I_D/I_G and I_{2D}/I_G ratios can be used to characterize LIG's structural properties.[43] According to the literature,[44] I_{2D}/I_G shows an exponential increase with defect concentration and can be classified as follows: $I_D/I_G \sim 2-3$, indicating highly defective graphene; $1< I_D/I_G < 2$, representing moderate defect levels; and $0 < I_D/I_G < 1$, indicating low defect levels or no defects. The 2D-to-G ratio indicates the layered nature of graphene, where $I_{2D}/I_G < 1$ signifies multilayered graphene stacks; $1< I_{2D}/I_G < 2$ relates to bilayer graphene; and $I_{2D}/I_G \sim 2-3$ corresponds to monolayers.[45] Figure 4d shows that LIG was formed at locations 1 and 2, with I_D/I_G ratios of 1.08 and 1.13, and I_{2D}/I_G ratios of 0.3 and 0.08, respectively.[46] Therefore, point 1's I_D/I_G ratio indicates moderately defective LIG, while the I_{2D}/I_G ratio suggests its multilayered structure. At point 2, the defectiveness of LIG increases, accompanied by a decrease in the I_{2D}/I_G ratio due to the weakening of the 2D band, indicating the beginning of the transition from LIG to amorphous carbon.[47] From locations 3 to 5, the D-peak's width and intensity increased, with no observable 2D peak, indicating the predominance of amorphous carbon in these areas.[47] By correlating the Raman results with high-speed recordings, we found that the thermal emission zones correspond to the locations of LIG and amorphous carbon (Figure 4c–d). Specifically, LIG forms exactly at the laser's impact point (the brightest thermal emission zone), while amorphous carbon forms at its periphery (red emission).

We continue the analysis similarly for the second case study: the laser scanning mode (Figure 4b). Because of the high laser power, a Cu-LIG forms. This process begins with CuNPs being ablated along the laser's path, which graphitizes the polymer. At the edges, the surrounding CuNPs sinter and become encapsulated by molten polymer. When the laser passes over the initially sintered CuNPs, heat dissipation causes other CuNPs to sinter around the beam track. High-speed recordings shown in Figure 4b, 150-ms frame, provide real-time evidence of the encapsulation process, demonstrating that as the laser moves, molten polymer from the trailing edge of the melt pool is drawn back over the sintered copper structures, leaving the central part of the laser path free of polymer (see also Supporting Video 6).

We hypothesize that the selective polymer encapsulation along the sides of the laser beam path results from a competition among different effects, dominated by local heating and high pressure in the molten pool. As the laser moves along, the thermal gradient causes Marangoni flows with polymer displacement away from the pool and over sintered CuNPs at the laser beam periphery.[48]

In contrast, the central line with LIG remains exposed, as shown by the carbon Raman peaks and the lack of PL background typical of molten PET, as depicted in Figure 4f and Figure S6. The absence of PET enabled us to assess the

https://doi.org/10.1021/acsami.5c17459
ACS Appl. Mater. Interfaces XXXX, XXX, XXX−XXX

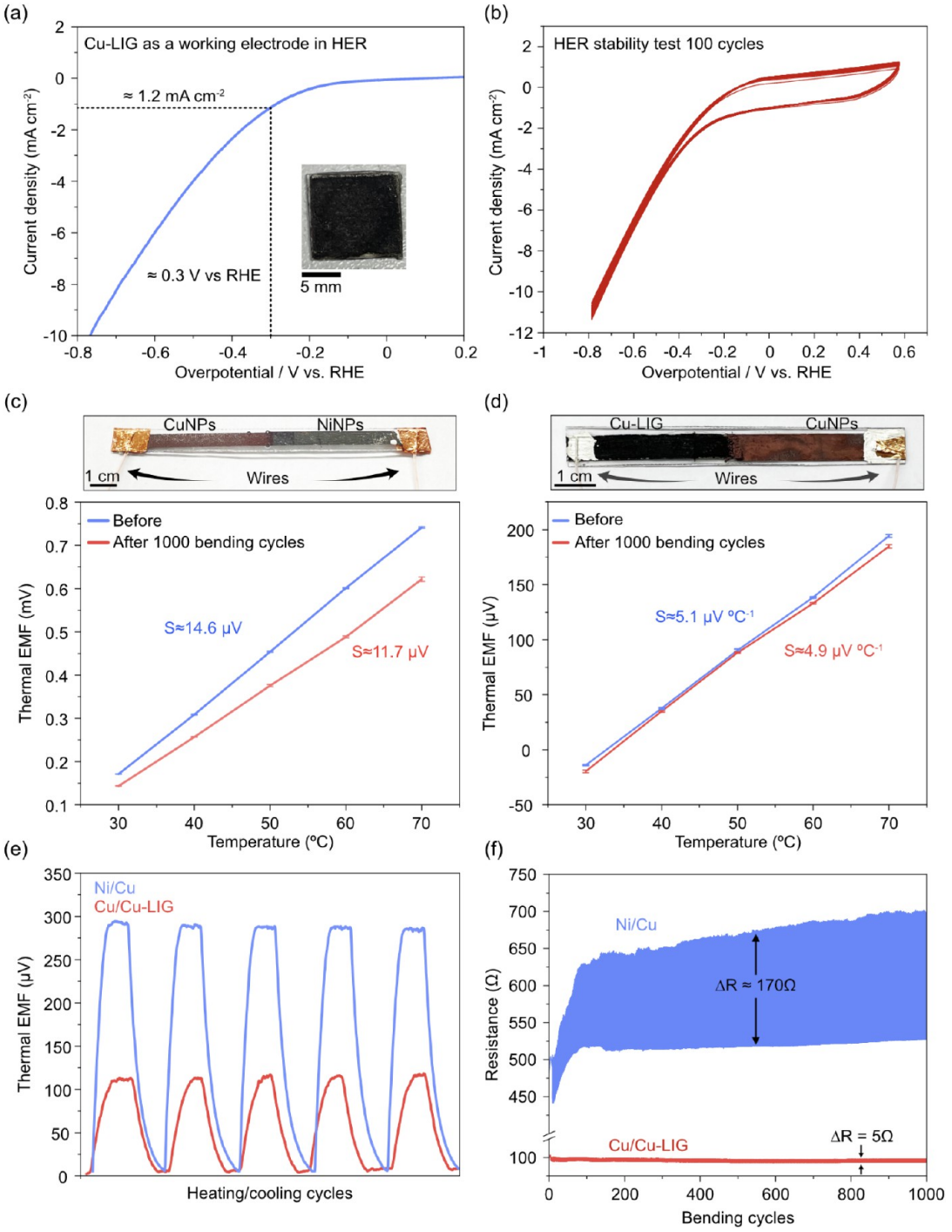

Figure 6. Composites' performance in HER and as thermocouples. (a) Cu-LIG as a working electrode in HER. (b) Stability test of Cu-LIG sample at 100 cycles of cyclic voltammetry. (c) Ni/Cu thermocouple and (d) Cu/Cu-LIG sensitivity plots before and after 1000 bending cycles. (e) Heating/cooling cycles from 25 to 50 °C. (f) 1000 bending cycles of Ni/Cu and Cu/Cu-LIG thermocouples, demonstrating a change in resistance of the thermocouples.

quality and structural properties of LIG from the center to the edge. Figure 4f–h present Raman spectra of the LIG center line with an I_D/I_G ratio of 0.67 and an I_{2D}/I_G ratio of 0.5, indicating multilayered LIG with low defect levels. Toward the edge, the I_D/I_G ratio increases to 1.78, suggesting a higher defect concentration in LIG. Simultaneously, the I_{2D}/I_G ratio drops to 0.11, due to reduced 2D band intensity, which indicates more amorphous carbon and less LIG.[49] The D and G peaks show small blue shifts in Figure 4g when moving from the center to the edge, while the 2D peak exhibits a red shift. However, the opposite shifts of the D and 2D peaks are likely due to fitting discrepancies rather than actual effects. The blue shift of the D peak reflects increased defect levels and compression strain,[50,51] whereas the red shift of the 2D mode suggests tensile strain. This indicates that both types of strain coexist within the structure. Furthermore, the Raman spectra from the spot (Figure 4c,d) and the line (Figure 4e–f) show different I_D/I_G ratios, with I_D/I_G(spot) > 1 and I_D/I_G(line) < 1,

https://doi.org/10.1021/acsami.5c17459
ACS Appl. Mater. Interfaces XXXX, XXX, XXX−XXX

as well as more prominent D+D″ and D+D′ peaks in the laser spot compared to the line. Given that the laser power and beam size were similar in both experiments, the defectiveness of LIG in our case depends on irradiation time (1 s for the spot vs 6 ms for the line), leading to overheating and more disordered carbon sheets.[46]

While a single laser-engraved line serves as a useful model for structural analysis, creating large-scale composites involves multiple line-by-line scans, which makes the process quite different. In this context, thermal spillover happens when heat and molten polymer from one line impact the adjacent line. High-speed recordings in Supporting Video 7 reveal that as the laser engraves a second line, the polymer spills over the first, encapsulating the LIG track with molten material. This shows that, unlike a single-line scan, large-area processing in a line-by-line manner leads to a polymer-encapsulated Cu-LIG hybrid composite.

SEM imaging results in Figure 5a,b show that the sample's shape heavily depends on the laser power. At lower power (644 mW, Figure 5a), the surface appears uneven with foam-like structures, while higher power (907 mW) creates a more even surface (Figure 5c). Raman spectra from the foam-like surface display overlapping LIG peaks and PET photoluminescence background.[34] In contrast, the uniform surface composite (Figure 5c,d) reveals much clearer LIG peaks without the usual PET background. The I_D/I_G ratios range from 0.47 to 1.24, and the presence of 2D bands in the spectra suggests the surface is made of multilayered LIG with low to moderate defect levels. Our observations indicate that large-scale samples consist of a mix of multilayered LIGs with varying defect densities.

The structural heterogeneity of LIG, caused by varying defect levels, results in differences in electronic properties and electrical conductivity across different regions within a sample. In individual structures (single spots or lines), these electronic properties are mainly influenced by variations in charge-carrier mobility. Previous studies have shown that charge-carrier mobility decreases as the defect concentration in LIG increases.[52] In heterogeneous structures, both the defect concentration and the type of carbon species (LIG or amorphous carbon) gradually change from the center to the periphery. Therefore, it is reasonable to expect a decrease in charge carrier mobility. In large-scale samples, this heterogeneity primarily appears as variations in sheet resistance. R_S values of our Cu-LIG hybrids ranged from 14.4 ± 2.9 Ω sq^{-1} to 21.6 ± 3.3 Ω sq^{-1}. In comparison, LIG derived from polyimide, a standard carbon precursor, typically shows R_S values of 15 Ω sq^{-1} or higher, depending on the laser processing conditions.[53] Meanwhile, lower R_S values, such as 8 Ω sq^{-1}, have been reported for LIG derived from wood.[54]

Copper NPs should also serve as important catalysts for LIG generation from PET, similar to their role in lignin.[55] Additionally, copper is a well-known catalyst in the chemical vapor deposition (CVD) process for graphene, facilitating pyrolysis, which is likely to happen in PET at high local temperatures.[56−58] The catalytic influence of copper can be roughly gauged by comparing our current findings with previous research,[4] where PET was laser carbonized by exposing it to an aluminum nanoparticle film on its surface. In that earlier study, PET carbonization was driven solely by photothermal effects, resulting in a conductive carbon network with a sheet resistance of 181 Ω sq^{-1}.[4] Conversely, our structures exhibit a sheet resistance two to 3 orders of magnitude lower, indicating that copper indeed plays a significant catalytic role.

In addition to LIG, optical microscopy (Figure 5e) showed Cu particles embedded in the composite. X-ray diffraction (Figure 5f) verified that the sample contains metallic Cu, with no Cu_2O or CuO phases. The lack of Cu oxides may result from graphene acting as a reducing agent for copper oxide, and the high temperature needed for LIG formation also promotes the reduction of Cu oxides.[45] Therefore, in this case, PVP's role as a reducing agent is minor, unlike in low-temperature processing, where Cu reduction mainly happens through PVP decomposition.

Applications in Flexible Electronics: From Water Splitting to Thermocouples. To assess the stability of the composite, we used a sample obtained at high laser power, LIG with incorporated Cu (Cu-LIG hereafter), as a working electrode for the hydrogen evolution reaction (HER) in 1 M KOH (pH 13.7). Although the Cu-LIG electrode showed modest HER activity (Figure 6a), with a current density of 1.2 mA cm^{-2} at 0.3 V (RHE), it demonstrated excellent durability and electrochemical stability. This electrode maintained stable performance for over 100 cycles (Figure 6b), confirming the composite's stability during electrochemical reactions. Additionally, despite the moderate HER performance, several strategies could further improve Cu-LIG's catalytic activity. For instance, heteroatom doping, including N, S, and P, can significantly influence the LIG kinetics of hydrogen evolution by modifying the electronic structure and increasing the number of active sites.[59,60] Another approach involves surface modification through creating additional defect sites, tuning the oxidation state of Cu, or introducing catalytically active metal species. All of these methods are known to accelerate water dissociation.[61,62]

It is worth noting that Cu-LIG offers several practical advantages, making it a suitable material for water electrolysis environments.[63] Its scalability, mechanical strength, and stable electrochemical behavior indicate that Cu-LIG could serve as a versatile and chemically durable electrode substrate that can be further modified to enhance catalytic activity.[64] Additionally, given the polymer−Cu composite chemistry and Cu's high selectivity for reducing CO_2 to hydrocarbons, this material could also be promising for other electrochemical reactions, mainly CO_2 reduction.[65]

To demonstrate the practical applications of the laser-driven sinter-then-encapsulate approach in flexible electronics, we fabricated thermocouples in two configurations: an encapsulated Ni/Cu device and a hybrid Cu/Cu-LIG device. The fabrication details are provided in the Supporting Information and shown in Figure S7. Both types of thermocouples exhibited good thermoelectric performance, as shown in Figure 6c,d for Ni/Cu and Cu/Cu-LIG, respectively. We increased the device temperature up to 70 °C and measured the thermal electromotive force (thermal EMF) as temperature changed, staying below the PET substrate's glass transition temperature, which occurs between 70 and 80 °C.

The Ni/Cu thermocouple showed a linear thermoelectric response with an average Seebeck coefficient of about 14.6 μV $°C^{-1}$, surpassing previously reported values of around 8.9 μV $°C^{-1}$ for magnetron-sputtered Cu and Ni devices on polyimide.[66] The Cu/Cu-LIG thermocouple displayed a sensitivity of 5.1 μV $°C^{-1}$, in agreement with calculations of the Seebeck coefficient difference between pure Cu (S = 6.5 μV $°C^{-1}$) and LIG (S varies between 4.73 and 12.77 μV

https://doi.org/10.1021/acsami.5c17459
ACS Appl. Mater. Interfaces XXXX, XXX, XXX−XXX

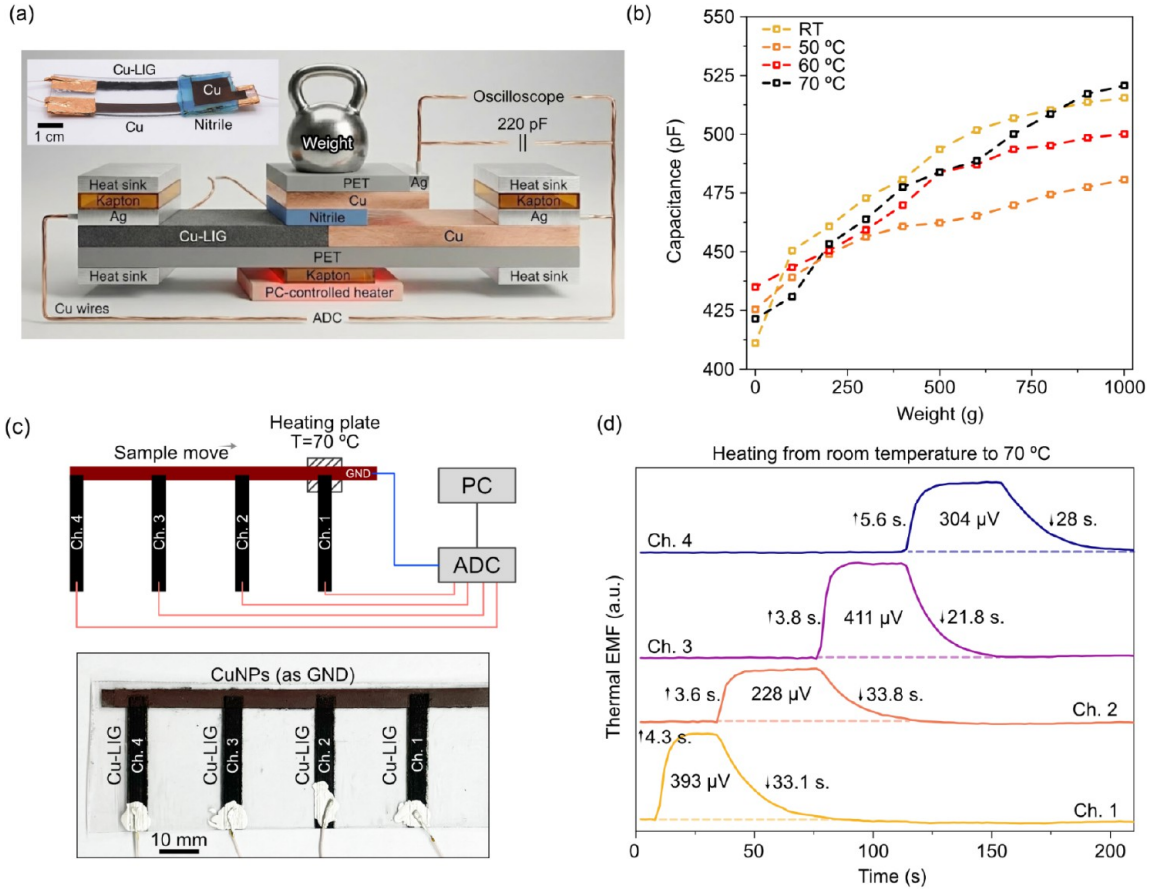

Figure 7. Temperature-pressure sensor and Cu/Cu-LIG thermocouple characteristics. (a) Scheme of the pressure-temperature sensor and the experimental setup. (b) Capacitance as a function of weight change. (c) Scheme of the thermocouple array and the experimental setup for temperature measurements. (d) Thermal EMF measured on different channels in the thermocouple array.

$°C^{-1}$).[67] Both configurations showed stable thermoelectric performance during repeated heating and cooling cycles from room temperature to 50 °C (Figure 6e). The key difference between the two devices was noted during mechanical resilience testing after 1000 bending cycles. Results in Figure 6f indicate that the Ni/Cu thermocouple was not mechanically durable, with resistance increasing from approximately 100 Ω to 400 Ω, and continuing to rise even after the test. Additionally, the resistance change (ΔR) increased from 60 Ω at the start to 170 Ω at the end of the bending cycles, indicating degradation. Conversely, the Cu/Cu-LIG hybrid composite showed only a slight resistance change from ΔR = 100 Ω to about 95 Ω. Therefore, the sensitivity of the Ni/Cu thermocouple decreased to 11.7 $\mu V\ °C^{-1}$ while the Cu/Cu-LIG dropped to 4.9 $\mu V\ °C^{-1}$.

We further demonstrate the multifunctionality of Cu/Cu-LIG thermocouples as dual-mode pressure-temperature sensors by integrating a capacitive sensor made of sintered Cu, as shown in Figure 7a. The device effectively decouples the two stimuli with minimal cross-talk across the temperature range of 27 to 70 °C. Capacitance changes in Figure 7b are on the order of dozens of pF and can support weights up to 1 kg. The small deviations in electrical capacitance across different temperatures are likely due to measurement inaccuracies rather than temperature effects. This is supported by the lack of a clear correlation between temperature increase and the sensor's capacitance.

We demonstrated the scalability of our approach by fabricating temperature-sensing arrays made of Cu/Cu-LIG thermocouples to map the surface thermal profile, as shown in Figure 7c. We tested the array device by moving a localized heat source and recording the thermal EMF response. The results in Figure 7d showed that the thermal EMF signal varied across channels, indicating differences in sensing performance. A proof-of-concept device displayed a thermocouple response with channel-to-channel variation, which could be due to both handmade contacts (expected to be the main factor in the observed variation) and uneven laser-induced heating caused by film inhomogeneity from drop-casting deposition (Note S1). Nevertheless, the lab-scale prototype demonstrated a successful application of the laser processing approach to produce thermocouple arrays.

The performance of a thermoelectric device is determined by the Seebeck coefficient (ZT) (1), which relies on the electrical and thermal conductivities of the system:

$$ZT = \frac{S^2\sigma}{\lambda}T \tag{1}$$

where S—Seebeck coefficient of the material, $\mu V\ °C^{-1}$; σ—electrical conductivity, S; λ—thermal conductivity, $W(m{\cdot}K)^{-1}$, and T—absolute temperature. In our Cu/Cu-LIG thermocouple array, performance is influenced not only by the intrinsic Seebeck coefficient and electrical conductivity of the thermoelectric materials but also by the low thermal conductivity of the polymer substrate. By optimizing key

https://doi.org/10.1021/acsami.5c17459
ACS Appl. Mater. Interfaces XXXX, XXX, XXX−XXX

parameters, such as using thinner substrates with higher thermal conductivity to enhance the device's figure of merit (ZT), we can improve both response time and sensitivity, making these proof-of-concept devices more suitable for thermal mapping applications. Besides the low thermal conductivity of the polymer substrate, the thermal behavior of the Cu-LIG layer aligns well with results reported for similar Cu-modified LIG systems. For example, a recent study shows that a Cu@hLIG/epoxy composite achieved a thermal conductivity of up to 16.4 W $m^{-1}K^{-1}$,[68] and another thermophysical study of sintering Cu NPs indicates their λ can increase from 18.5 to 26.8 W $m^{-1}K^{-1}$.[36] These reports suggest that Cu-LIG structures with sintered Cu NPs can be expected to exhibit thermal conductivities on the order of 15−30 W $m^{-1}K^{-1}$. At the same time, in our composite, the heat flow is limited by the PET substrate, whose thermal conductivity is much lower (0.15−0.25 W $m^{-1}K^{-1}$). Therefore, the exact value of λ for the Cu-LIG layer has a relatively minor effect on the overall ZT analysis. In this context, the substrate limitation stems from its thermoplastic nature for such laser-driven composites, as reported by Abyzova et al.[5]

CONCLUSIONS

In summary, this work presents a novel laser-based manufacturing platform that goes beyond the traditional selective laser sintering approach to tackle key challenges in processing copper nanoparticles on polymer substrates under ambient conditions. By adjusting the laser processing parameters, we can control the transformation of a single precursor into either an oxide-free, conductive CuNPs/PET composite stabilized by in situ polymer encapsulation or a Cu-assisted laser-induced graphene (Cu-LIG) hybrid embedded within the substrate. Encapsulated Cu structures showed excellent performance, with a minimal sheet resistance of 0.13 Ω sq^{-1}, and strong stability under both tough and mild cycling conditions. The top-performing sample, without additional protective layers, maintained R_S values from 3.4 ± 1.7 Ω sq^{-1} (initial) to 5.5 ± 1.8 Ω sq^{-1} after aging. In comparison, Cu-LIG hybrids exhibited R_S values from 14.4 ± 2.9 Ω sq^{-1} to 21.6 ± 3.3 Ω sq^{-1}, which are comparable to those of LIG produced from polyimide. High-speed visualization, FEM simulations, and structural analyses uncovered the mechanisms behind nanoparticle sintering, encapsulation, reduction, and polymer integration. Unlike previous reports on laser processing of metallic nanoparticles, our method offers a one-step process that ensures conductivity, oxide reduction, strong adhesion to the substrate, and environmental protection simultaneously. The encapsulation strategy provided excellent stability against oxidation and high humidity, while the Cu-LIG can serve as a hybrid carbon−metal electrode in the HER reaction, demonstrating remarkable stability over 100 electrochemical cycles. A wide range of functionalities was showcased in Ni/Cu and Cu/Cu-LIG thermocouples, with maximum sensitivities of 14.6 μV $°C^{-1}$ and 5.1 μV $°C^{-1}$, respectively; pressure-temperature sensors; and thermocouple arrays.

Despite its advantages, our method has important limitations. Nanomaterial encapsulation through laser-induced melting mainly works with thermoplastic polymers. Thermosetting polymers, because of irreversible cross-linking, are not suitable for encapsulation and may instead degrade or become graphitized. This limits the substrates we can use, particularly for high-temperature applications like polyimides. This presents an opportunity for future research: developing laser-processing techniques for thermosetting polymers. Additionally, future work should focus on reducing cracks in bent CuNP films and enhancing batch consistency. Overcoming these challenges will help advance the development of next-generation flexible electronics.

MATERIALS AND METHODS

Sample Preparation. Commercially available CuNPs and NiNPs (Advanced Powder Technologies, Russia) were used for this work. 50 mg of CuNPs was dispersed in 3 mg of PVP with 1 mL of EtOH, then sonicated for 1 h in an ultrasonic bath. Next, using the drop-casting method, CuNPs were applied to a PET substrate at a concentration of 50 μL cm^{-2}. Finally, the sample was dried in ambient conditions or, alternatively, on a heating plate at 40−45 °C. The average thickness of the CuNPs film after drying was 5 μm. The detailed preparation of thermocouples is shown in Figure S7. The NiNPs dispersion was prepared under the same conditions and at the same concentration. For cross-section SEM investigation, samples were broken in liquid nitrogen.

Laser Processing and High-Speed Recordings. For the case of CuNPs laser-induced encapsulation, laser processing was performed using a 450 nm CW laser with a 30 × 30 μm top-hat laser beam. The laser beam power was controlled electronically. Irradiation was performed with a 10× objective equipped with a 0.28 NA aperture. The sample processing was performed on an XY motorized stage that moved at 5 mm s^{-1} (OMTOOLS, China). Laser processing was recorded with a high-speed camera (Phantom Miro C110, USA) at 500 fps (Supporting Video 4), 1200 fps (Supporting Video 1), and 1900 fps (Supporting Videos 2 and 3). For the formation of Cu-LIG, laser processing used a 438 nm laser at 600 mW in a pulsed regime with a 1 kHz pulse frequency and 900 μs pulse duration. Cu-LIG processing either at a fixed spot or while moving (Supporting Videos 5 and 6) was recorded at 1200 fps, while laser scanning (Supporting Video 7) was recorded at 1600 fps.

Raman Spectroscopy. Raman spectroscopy was done using the NTEGRA Spectra II AFM-Raman system (NT-MDT, Russia) using a 532 nm CW laser at 100× magnification.

SEM Imaging. SEM imaging, including top view and cross-section images, was done using COXEM EM-30 PLUS (South Korea) at a 7 kV acceleration speed.

X-ray Diffraction Measurements. XRD patterns were obtained using Shimadzu XRD 7000S in a Bragg−Brentano configuration with CuKα tube (40 kV, 30 mA). Scanning range has been set from 10 to 80° at a scanning speed of 10° min^{-1} and 0.0143° step.

Electrical and Thermoelectric Parameters Measurements. I(V) characteristics and bending tests with 20 mm bending radius were conducted using a Corrtest CS 2350 bipotentiostat. The thermoelectric response was measured using an ADC converter (L-CARD E-502, Russia). The sample was heated by a heating plate supplied with the NTEGRA Spectra II AFM-Raman system.

FEM Simulations. Laser heating simulation of the Cu NPs film on PET was conducted using COMSOL Multiphysics software. The Heat Transfer in the Solids module was utilized. The continuous laser heating was modeled as a fixed heat source at the center of the sample surface. The sample dimensions were set to 1 mm in width and length, with a 1 μm Cu NPs film on a 0.7 mm PET substrate. A parametric sweep

https://doi.org/10.1021/acsami.5c17459
ACS Appl. Mater. Interfaces XXXX, XXX, XXX−XXX

of laser power was performed from 30 to 70 mW in 10 mW steps. The laser spot size was specified as 30 μm × 30 μm with a top-hat power distribution. Laser heating time ranged from 0 to 400 ms. All parameters were selected based on experimental measurements to closely replicate the experimental conditions, enabling a comprehensive comparison between experimental and theoretical data.

■ ASSOCIATED CONTENT

Data Availability Statement

Data are provided within this manuscript and the Supporting Information files.

Supporting Information

The Supporting Information is available free of charge at https://pubs.acs.org/doi/10.1021/acsami.5c17459.

Sheet-resistance data; optical images and Raman spectra; absorption and XRD measurements; photoluminescence background; NiNPs and CuNPs sintering/encapsulation results; flexible thermocouple fabrication scheme and notes; high-speed video recordings (PDF)

Laser processing of CuNPs in a single spot reveals sintering and encapsulation stages (Video S1) (MP4)

Laser processing of CuNPs in a single spot demonstrating the integration of sintered CuNPs (Video S2) (MP4)

Laser engraving of a single line with CuNPs sintering and encapsulation (Video S3) (MP4)

Line-by-line laser scanning process of CuNPs (Video S4) (MP4)

LIG formation process in a single spot (Video S5) (MP4)

LIG formation during single line laser processing (Video S6) (MP4)

Line-by-line laser processing, showing with LIG formation and encapsulation of previously formed LIG structure (Video S7) (MP4)

■ AUTHOR INFORMATION

Corresponding Author

Raul D. Rodriguez − *Tomsk Polytechnic University, Tomsk 634050, Russia;* orcid.org/0000-0003-4016-1469; Email: raul@tpu.ru

Authors

Dmitry Cheshev − *Tomsk Polytechnic University, Tomsk 634050, Russia*

Sergey Kaprov − *Tomsk Polytechnic University, Tomsk 634050, Russia*

Andrey Averkiev − *Tomsk Polytechnic University, Tomsk 634050, Russia*

Maxim Fatkullin − *Tomsk Polytechnic University, Tomsk 634050, Russia*

Konstantin Brazovskiy − *Tomsk Polytechnic University, Tomsk 634050, Russia*

Evgeniya Sheremet − *Tomsk Polytechnic University, Tomsk 634050, Russia;* orcid.org/0000-0003-3937-8628

Complete contact information is available at: https://pubs.acs.org/10.1021/acsami.5c17459

Author Contributions

D.C.: Project administration, Conceptualization, Methodology, Data curation, Formal analysis, Writing—original draft. S.K.: Data curation, Formal analysis, Writing—original draft, review and editing. A.A.: FEM simulations, Formal analysis, Writing—original draft, review and editing. M.F.: Data curation, Formal analysis, Writing—review and editing. K.B.: Supervision, Methodology, Writing—review and editing. R.D.R.: Supervision, Conceptualization, Methodology, Writing—original draft, reviewing and editing. E.S.: Supervision, Conceptualization, Methodology, Writing—review and editing, Funding acquisition.

Notes

The authors declare no competing financial interest.

■ ACKNOWLEDGMENTS

We acknowledge funding from the RSF grant no. 23-42-00081 and are grateful for the scientific equipment and facilities provided by the Tomsk Polytechnic University. We appreciate Stepanov S.A. for providing the optical equipment for diffuse-reflectance spectra measurements and Syrtanov M.S. for the XRD experiments.

■ REFERENCES

(1) Zenou, M.; Ermak, O.; Saar, A.; Kotler, Z. Laser Sintering of Copper Nanoparticles. *J. Phys. D Appl. Phys.* **2014**, *47* (2), 025501.

(2) Tian, Y.; Jiang, Z.; Wang, C.; Ding, S.; Wen, J.; Liu, Z.; Wang, C. Sintering Mechanism of the Cu−Ag Core−shell Nanoparticle Paste at Low Temperature in Ambient Air. *RSC Adv.* **2016**, *6* (94), 91783−91790.

(3) Baimler, I. V.; Simakin, A. V.; Dorokhov, A. S.; Gudkov, S. V. Mini-Review on Laser-Induced Nanoparticle Heating and Melting. *Front. Chem.* **2024**, *12*, 1463612.

(4) Rodriguez, R. D.; Shchadenko, S.; Murastov, G.; Lipovka, A.; Fatkullin, M.; Petrov, I.; Tran, T.-H.; Khalelov, A.; Saqib, M.; Villa, N. E.; et al. Ultra-robust Flexible Electronics by Laser-driven Polymer-nanomaterials Integration. *Adv. Funct. Mater.* **2021**, *31* (17), 2008818.

(5) Abyzova, E.; Petrov, I.; Bril', I.; Cheshev, D.; Ivanov, A.; Khomenko, M.; Averkiev, A.; Fatkullin, M.; Kogolev, D.; Bolbasov, E.; Matkovic, A.; Chen, J.-J.; Rodriguez, R. D.; Sheremet, E. Universal Approach to Integrating Reduced Graphene Oxide into Polymer Electronics. *Polymers* **2023**, *15* (24), 4622.

(6) Fatkullin, M.; Rodriguez, R. D.; Petrov, I.; Villa, N. E.; Lipovka, A.; Gridina, M.; Murastov, G.; Chernova, A.; Plotnikov, E.; Averkiev, A.; Cheshev, D.; Semyonov, O.; Gubarev, F.; Brazovskiy, K.; Sheng, W.; Amin, I.; Liu, J.; Jia, X.; Sheremet, E. Molecular Plasmonic Silver Forests for the Photocatalytic-Driven Sensing Platforms. *Nanomaterials* **2023**, *13* (5), 923.

(7) Shen, T.; Liu, Y.; Zhu, Y.; Yang, D.-Q.; Sacher, E. Improved Adhesion of Ag NPs to the Polyethylene Terephthalate Surface via Atmospheric Plasma Treatment and Surface Functionalization. *Appl. Surf. Sci.* **2017**, *411*, 411−418.

(8) Tharchanaa, S. B.; Anupriyanka, T.; Shanmugavelayutham, G. Ecofriendly Surface Modification of Cotton Fabric to Enhance the Adhesion of CuO Nanoparticles for Antibacterial Activity. *Mater. Technol.* **2022**, *37* (14), 3222−3230.

(9) Fortunati, E.; Mattioli, S.; Visai, L.; Imbriani, M.; Fierro, J. L. G.; Kenny, J. M.; Armentano, I. Combined Effects of Ag Nanoparticles and Oxygen Plasma Treatment on PLGA Morphological, Chemical, and Antibacterial Properties. *Biomacromolecules* **2013**, *14* (3), 626−636.

(10) Rahman, M. T.; Cheng, C.-Y.; Karagoz, B.; Renn, M.; Schrandt, M.; Gellman, A.; Panat, R. High Performance Flexible Temperature Sensors via Nanoparticle Printing. *ACS Appl. Nano Mater.* **2019**, *2* (5), 3280−3291.

(11) Tomotoshi, D.; Kawasaki, H. Surface and Interface Designs in Copper-Based Conductive Inks for Printed/Flexible Electronics. *Nanomaterials* **2020**, *10* (9), 1689.

(12) Chen, X.; Zhang, M.; Zhu, J.; Tao, Z.; Qiu, L. Laser Sintering of Cu Nanoparticles Deposited on Ceramic Substrates: Experiments and Modeling. *Addit. Manuf.* **2023**, *69*, 103527.
(13) Yu, J. H.; Kang, K.-T.; Hwang, J. Y.; Lee, S.-H.; Kang, H. Rapid Sintering of Copper Nano Ink Using a Laser in Air. *Int. J. Precis. Eng. Manuf.* **2014**, *15* (6), 1051−1054.
(14) Kwon, J.; Cho, H.; Eom, H.; Lee, H.; Suh, Y. D.; Moon, H.; Shin, J.; Hong, S.; Ko, S. H. Low-Temperature Oxidation-Free Selective Laser Sintering of Cu Nanoparticle Paste on a Polymer Substrate for the Flexible Touch Panel Applications. *ACS Appl. Mater. Interfaces* **2016**, *8* (18), 11575−11582.
(15) Yasuda, K.; Takada, Y.; Song, J.-M. Characterization of Additively Formed Copper Layer by Blue Laser-Sintered Copper Nanoparticles. In *2021 International Conference on Electronics Packaging (ICEP)*; IEEE: Tokyo, Japan, 2021, pp. 53-54.
(16) Cho, C. H.; Shin, I. K.; Kim, K. Y.; Choi, Y. J. Enhancing Adhesion Properties between Binder-Free Copper Nanoink and Flexible Substrate Using Chemically Generated Interlocking Structure. *Appl. Surf. Sci.* **2019**, *485*, 484−489.
(17) Dayss, E.; Leps, G.; Meinhardt, J. Surface Modification for Improved Adhesion of a Polymer−metal Compound. *Surf. Coat. Technol.* **1999**, *116*−*119*, 986−990.
(18) Yokoyama, S.; Nozaki, J.; Motomiya, K.; Tsukahara, N.; Takahashi, H. Strong Adhesion of Polyvinylpyrrolidone-Coated Copper Nanoparticles on Various Substrates Fabricated from Well-Dispersed Copper Nanoparticle Inks. *Colloids Surf. A* **2020**, *591*, 124567.
(19) Zhang, D.; Gökce, B. Perspective of Laser-Prototyping Nanoparticle-Polymer Composites. *Appl. Surf. Sci.* **2017**, *392*, 991−1003.
(20) Sekine, T.; Fukuda, K.; Kumaki, D.; Tokito, S. Enhanced Adhesion Mechanisms between Printed Nano-Silver Electrodes and Underlying Polymer Layers. *Nanotechnology* **2015**, *26* (32), 321001.
(21) Kwon, Y.-T.; Kim, Y.-S.; Lee, Y.; Kwon, S.; Lim, M.; Song, Y.; Choa, Y.-H.; Yeo, W.-H. Ultrahigh Conductivity and Superior Interfacial Adhesion of a Nanostructured, Photonic-Sintered Copper Membrane for Printed Flexible Hybrid Electronics. *ACS Appl. Mater. Interfaces* **2018**, *10* (50), 44071−44079.
(22) Peng, J.; Chen, B.; Wang, Z.; Guo, J.; Wu, B.; Hao, S.; Zhang, Q.; Gu, L.; Zhou, Q.; Liu, Z.; Hong, S.; You, S.; Fu, A.; Shi, Z.; Xie, H.; Cao, D.; Lin, C.-J.; Fu, G.; Zheng, L.-S.; Jiang, Y.; Zheng, N. Surface Coordination Layer Passivates Oxidation of Copper. *Nature* **2020**, *586* (7829), 390−394.
(23) Mock, J.; Bobinger, M.; Bogner, C.; Lugli, P.; Becherer, M. Aqueous Synthesis, Degradation, and Encapsulation of Copper Nanowires for Transparent Electrodes. *Nanomaterials* **2018**, *8* (10), 767.
(24) Wang, J.; Zhang, Z.; Wang, S.; Zhang, R.; Guo, Y.; Cheng, G.; Gu, Y.; Liu, K.; Chen, K. Superstable Copper Nanowire Network Electrodes by Single-Crystal Graphene Covering and Their Applications in Flexible Nanogenerator and Light-Emitting Diode. *Nano Energy* **2020**, *71*, 104638.
(25) Shin, D.; Choi, S.; Eunkyung Kim, S.; Yun, C.; Yee Tan, Y.; Sunyong Lee, C. Fabrication of Multilayer Graphene-Coated Copper Nanoparticles for Application as a Thermal Interface Material. *Appl. Surf. Sci.* **2022**, *583*, 152488.
(26) Cheng, K.; Xiong, W.; Li, Y.; Hao, L.; Yan, C.; Li, Z.; Liu, Z.; Wang, Y.; Essa, K.; Lee, L.; Gong, X.; Peijs, T. In-Situ Deposition of Three-Dimensional Graphene on Selective Laser Melted Copper Scaffolds for High Performance Applications. *Composites, Part A* **2020**, *135*, 105904.
(27) Liao, J.; Guo, W.; Peng, P. Direct Laser Writing of Copper-Graphene Composites for Flexible Electronics. *Opt. Lasers Eng.* **2021**, *142*, 106605.
(28) Luo, B.; Xuan, S.; Wang, X.; Ding, K.; Jin, P.; Zheng, Y.; Wu, Z. Liposome/chitosan Coating Film Bioplastic Packaging for Litchi Fruit Preservation. *Food Chem.* **2025**, *464* (Pt 3), 141850.
(29) Wu, Y.; Zou, G.; Wang, S.; Guo, W.; Zhang, H.; Liu, L. Interfacial Bonding Mechanisms of Sintered Cu Nanoparticles on Different Metallization Surfaces. *Surf. Interfaces* **2024**, *46*, 104173.
(30) Pereira, H. J.; Makarovsky, O.; Amabilino, D. B.; Newton, G. N. Room Temperature Compressed Air-Stable Conductive Copper Films for Flexible Electronics. *Npj Flexible Electron.* **2024**, *8* (1), 44.
(31) Joo, M.; Lee, B.; Jeong, S.; Lee, M. Laser Sintering of Cu Paste Film Printed on Polyimide Substrate. *Appl. Surf. Sci.* **2011**, *258* (1), 521−524.
(32) Hernandez-Castaneda, J. C.; Lok, B. K.; Zheng, H. Laser Sintering of Cu Nanoparticles on PET Polymer Substrate for Printed Electronics at Different Wavelengths and Process Conditions. *Front. Mech. Eng.* **2020**, *15* (2), 303−318.
(33) Huang, Y.; Xie, X.; Li, M.; Xu, M.; Long, J. Copper Circuits Fabricated on Flexible Polymer Substrates by a High Repetition Rate Femtosecond Laser-Induced Selective Local Reduction of Copper Oxide Nanoparticles. *Opt. Express* **2021**, *29* (3), 4453−4463.
(34) Petrov, I.; Rodriguez, R. D.; Frantsina, E. V.; Grinko, A.; Sheremet, E. Transforming Oil Waste into Highly Conductive Composites: Enabling Flexible Electronics through Laser Processing of Asphaltenes. *Adv. Compos. Hybrid Mater.* **2024**, *7* (2), 41.
(35) Jiaqi, L.; Haifang, N.; Chen, W.; Qingquan, L. Photoluminescence Measurement of Poly (ethylene Terephthalate) Films. In *2009 IEEE 9th International Conference on the Properties and Applications of Dielectric Materials*; IEEE: Harbin, 2009.
(36) Jeong, J.; Wang, Y. Thermal Properties of Copper Nanoparticles at Different Sintering Stages Governed by Nanoscale Heat Transfer. *Addit. Manuf. Lett.* **2023**, *4*, 100114.
(37) Bajtošová, L.; Kihoulou, B.; Králík, R.; Hanuš, J.; Cieslar, M. Nickel Nanoparticles: Insights into Sintering Dynamics. *Crystals* **2024**, *14* (4), 321.
(38) Groeninckx, G.; Reynaers, H.; Berghmans, H.; Smets, G. Morphology and Melting Behavior of Semicrystalline Poly(ethylene Terephthalate). I. Isothermally Crystallized PET. *J. Polym. Sci. Polym. Phys. Ed.* **1980**, *18* (6), 1311−1324.
(39) Lam, N.; Smith, R.; Le, N.; Thuy, C.; Tamboli, M.; Tamboli, A.; Alshehri, S.; Ghoneim, M.; Truong, N.; Jung, J. Evaluation of the Structural Deviation of Cu/Cu_2O Nanocomposite Using the X-Ray Diffraction Analysis Methods. *Crystals* **2022**, *12* (4), 566.
(40) Korshunov, A. V.; Il'in, A. P. Oxidation of Copper Nanopowders on Heating in Air. *Russian J. Appl. Chem.* **2009**, *82* (7), 1164−1171.
(41) Lee, H.; Yang, M. Effect of Solvent and PVP on Electrode Conductivity in Laser-Induced Reduction Process. *Appl. Phys. A* **2015**, *119* (1), 317−323.
(42) Ryu, J.; Kim, H.-S.; Hahn, H. T. Reactive Sintering of Copper Nanoparticles Using Intense Pulsed Light for Printed Electronics. *J. Electron. Mater.* **2011**, *40* (1), 42−50.
(43) Lin, J.; Peng, Z.; Liu, Y.; Ruiz-Zepeda, F.; Ye, R.; Samuel, E. L. G.; Yacaman, M. J.; Yakobson, B. I.; Tour, J. M. Laser-Induced Porous Graphene Films from Commercial Polymers. *Nat. Commun.* **2014**, *5*, 5714.
(44) Jorio, A.; Ferreira, E. H. M.; Moutinho, M. V. O.; Stavale, F.; Achete, C. A.; Capaz, R. B. Measuring Disorder in Graphene with the G and D Bands. *Phys. Status Solidi B* **2010**, *247* (11−12), 2980−2982.
(45) Nguyen, V. T.; Le, H. D.; Nguyen, V. C.; Tam Ngo, T. T.; Le, D. Q.; Nguyen, X. N.; Phan, N. M. Synthesis of Multi-Layer Graphene Films on Copper Tape by Atmospheric Pressure Chemical Vapor Deposition Method. *Adv. Nat. Sci. Nanosci. Nanotechnol* **2013**, *4* (3), 035012.
(46) Nasraoui, S.; Al-Hamry, A.; Madeira, T. I.; Ameur, S.; Zahn, D. R. T.; Ben Ali, M.; Kanoun, O. Structural Characterization and Electrochemical Performance of Laser-Induced Graphene: Insights into Electron Transfer Kinetics and 4-Aminophenol Sensing. *Diamond Relat. Mater.* **2023**, *138*, 110207.
(47) Das, A.; Chakraborty, B.; Sood, A. K. Raman Spectroscopy of Graphene on Different Substrates and Influence of Defects. *Bull. Mater. Sci.* **2008**, *31* (3), 579−584.

https://doi.org/10.1021/acsami.5c17459
ACS Appl. Mater. Interfaces XXXX, XXX, XXX−XXX

(48) Lee, Y. S.; Zhang, W. Modeling of Heat Transfer, Fluid Flow and Solidification Microstructure of Nickel-Base Superalloy Fabricated by Laser Powder Bed Fusion. *Addit. Manuf.* **2016**, *12*, 178−188.
(49) Ferrari, A. C.; Robertson, J. Resonant Raman spectroscopy of disordered, amorphous, and diamondlike carbon. *Phys. Rev. B* **2001**, *64*, 075414.
(50) Zheng, X.; Chen, W.; Wang, G.; Yu, Y.; Qin, S.; Fang, J.; Wang, F.; Zhang, X.-A. The Raman Redshift of Graphene Impacted by Gold Nanoparticles. *AIP Adv.* **2015**, *5* (5), 057133.
(51) Ott, A. K.; Ferrari, A. C. Raman Spectroscopy of Graphene and Related Materials. *Encyclopedia of Condensed Matter Physics*; Elsevier, 2024, pp.233−247.
(52) Chen, L.; Li, N.; Yu, X.; Zhang, S.; Liu, C.; Song, Y.; Li, Z.; Han, S.; Wang, W.; Yang, P.; et al. A General Way to Manipulate Electrical Conductivity of Graphene. *Chem. Eng. J.* **2023**, *462*, 142139.
(53) Le, T.-S. D.; Phan, H.-P.; Kwon, S.; Park, S.; Jung, Y.; Min, J.; Chun, B. J.; Yoon, H.; Ko, S. H.; Kim, S.-W.; et al. Recent Advances in Laser-induced Graphene: Mechanism, Fabrication, Properties, and Applications in Flexible Electronics. *Adv. Funct. Mater.* **2022**, *32* (48), 2205158.
(54) Chyan, Y.; Ye, R.; Li, Y.; Singh, S. P.; Arnusch, C. J.; Tour, J. M. Laser-Induced Graphene by Multiple Lasing: Toward Electronics on Cloth, Paper, and Food. *ACS Nano* **2018**, *12* (3), 2176−2183.
(55) Leng, W.; Barnes, H. M.; Cai, Z.; Zhang, J. Temperature and Copper Concentration Effects on the Formation of Graphene-Encapsulated Copper Nanoparticles from Kraft Lignin. *Materials* **2017**, *10* (6), 677.
(56) Bhaviripudi, S.; Jia, X.; Dresselhaus, M. S.; Kong, J. Role of Kinetic Factors in Chemical Vapor Deposition Synthesis of Uniform Large Area Graphene Using Copper Catalyst. *Nano Lett.* **2010**, *10* (10), 4128−4133.
(57) Kidambi, P. R.; Bayer, B. C.; Blume, R.; Wang, Z.-J.; Baehtz, C.; Weatherup, R. S.; Willinger, M.-G.; Schloegl, R.; Hofmann, S. Observing Graphene Grow: Catalyst-Graphene Interactions during Scalable Graphene Growth on Polycrystalline Copper. *Nano Lett.* **2013**, *13* (10), 4769−4778.
(58) Choi, D. S.; Kim, K. S.; Kim, H.; Kim, Y.; Kim, T.; Rhy, S.-H.; Yang, C.-M.; Yoon, D. H.; Yang, W. S. Effect of Cooling Condition on Chemical Vapor Deposition Synthesis of Graphene on Copper Catalyst. *ACS Appl. Mater. Interfaces* **2014**, *6* (22), 19574−19578.
(59) Zhang, Q.; Zhang, F.; Liu, X.; Yue, Z.; Chen, X.; Wan, Z. Doping of Laser-induced Graphene and Its Applications. *Adv. Mater. Technol.* **2023**, *8* (16), 2300244.
(60) Hung, Y.-H.; Dutta, D.; Tseng, C.-J.; Chang, J.-K.; Bhattacharyya, A. J.; Su, C.-Y. Manipulation of Heteroatom Substitution on Nitrogen and Phosphorus Co-Doped Graphene as a High Active Catalyst for Hydrogen Evolution Reaction. *J. Phys. Chem. C* **2019**, *123* (36), 22202−22211.
(61) Zhang, J.; Zhang, C.; Sha, J.; Fei, H.; Li, Y.; Tour, J. M. Efficient Water-Splitting Electrodes Based on Laser-Induced Graphene. *ACS Appl. Mater. Interfaces* **2017**, *9* (32), 26840−26847.
(62) de Almeida, J. C.; Wang, Y.; Rodrigues, T. A.; Nunes, P. H. H.; de Mendonça, V. R.; Falsetti, P. H. E.; Savazi, L. V.; He, T.; Bardakova, A. V.; Rudakova, A. V.; Tian, J.; Emeline, A. V.; Lopes, O. F.; Patrocínio, A. O. T.; Pan, J. H.; Ribeiro, C.; Bahnemann, D. W. Copper-based Materials for Photo and Electrocatalytic Process: Advancing Renewable Energy and Environmental Applications. *Adv. Funct. Mater.* **2025**, 2502901.
(63) Lopes, D. V.; Santos, N. F.; Moura, J. P.; Fernandes, A. J. S.; Costa, F. M.; Kovalevsky, A. V. Design of Laser-Induced Graphene Electrodes for Water Splitting. *Int. J. Hydrogen Energy* **2023**, *48* (11), 4158−4172.
(64) Murastov, G.; Bogatova, E.; Brazovskiy, K.; Amin, I.; Lipovka, A.; Dogadina, E.; Cherepnyov, A.; Ananyeva, A.; Plotnikov, E.; Ryabov, V.; Rodriguez, R. D.; Sheremet, E. Flexible and Water-Stable Graphene-Based Electrodes for Long-Term Use in Bioelectronics. *Biosens Bioelectron.* **2020**, *166*, 112426.
(65) Kok, J.; Albertini, P. P.; Leemans, J.; Buonsanti, R.; Burdyny, T. Overcoming Copper Stability Challenges in CO2 Electrolysis. *Nat. Rev. Mater.* **2025**, *10*, 550.
(66) Martiny, N.; Rheinfeld, A.; Geder, J.; Wang, Y.; Kraus, W.; Jossen, A. Development of an All Kapton-Based Thin-Film Thermocouple Matrix for in Situ Temperature Measurement in a Lithium Ion Pouch Cell. *IEEE Sens. J.* **2014**, *14* (10), 3377−3384.
(67) Kincal, C.; Solak, N. Controlling Thermoelectric Properties of Laser-Induced Graphene on Polyimide. *Nanomaterials* **2024**, *14* (10), 879.
(68) Yu, Z.; Zhao, W.; Mu, M.; Chen, G.; Yu, W.; Liu, X. Highly Thermal Conductive Epoxy Composites Enabled by 3D graphene/Cu-Based Dual Networks for Efficient Thermal Management. *Compos. Commun.* **2024**, *46*, 101845.

https://doi.org/10.1021/acsami.5c17459
ACS Appl. Mater. Interfaces XXXX, XXX, XXX−XXX